



Nickel metaphosphate supported ruthenium for all pH hydrogen evolution: From single atom, cluster to nanoparticle

Dewen Wang^a, Dongxu Jiao^a, Ming Gong^a, Huafeng Fan^a, Yuting Chen^c, Lezhi Wang^a, Jinchang Fan^a, Jiandong Wu^a, David J. Singh^{a,d}, Jingxiang Zhao^{b,*}, Weitao Zheng^{a,*}, Xiaoqiang Cui^{a,*}

^a State Key Laboratory of Automotive Simulation and Control, School of Materials Science and Engineering, Key Laboratory of Automobile Materials of MOE, Jilin Provincial International Cooperation Key Laboratory of High-Efficiency Clean Energy Materials, Electron Microscopy Center, Jilin University, Changchun 130012, PR China

^b Key Laboratory of Photonic and Electronic Bandgap Materials, Ministry of Education, and College of Chemistry and Chemical Engineering, Harbin Normal University, Harbin 150025, PR China

^c State Key Laboratory of Electroanalytical Chemistry, Changchun Institute of Applied Chemistry, Chinese Academy of Sciences, Changchun 130022, PR China

^d Department of Physics and Astronomy and Department of Chemistry, University of Missouri, Columbia, MO 65211, United States

ARTICLE INFO

Keywords:

Hydrogen evolution reactions
Metal-support interactions
Size effect
Single atom and nanoparticle
All pH conditions

ABSTRACT

Single-atom catalysts have attracted extensive attention due to their unique performances and high atom utilization. However, is single atom always the best? Here we found a reverse case that nickel metaphosphate (NPO) supported nanoparticles (Ru_n) is much better than single atoms (Ru_s) for all pH hydrogen evolution. The mass activity of Ru_n -NPO is 3.8 times higher than that of Ru_s -NPO, and 21.4 times higher than that of Pt/C in alkaline media. The results show that Ru nanoparticle possess lower valence state than single atom, providing optimized Ru-H bond strength and suitable hydrogen adsorption free energy. As a novel support, NPO is also essential for firmly anchoring Ru and transporting electrons for optimizing the *d*-band center, and eventually accelerating the H_2O dissociation in rate-limiting Volmer step. This work gives Ru-NPO promising potential for practical hydrogen production, and sheds light on the exploration of supported metal catalysts in energy conversion-related fields.

1. Introduction

As a special supported metal catalyst, single-atom catalysts are currently a research hotspot in the field of catalysis, and are widely used in water electrolysis and other fields [1–6]. It exhibits unique advantages in elucidating the structure-activity relationship and maximizing atom utilization, especially for the cost reduction of noble metals [7–10]. However, there is still interrogatory of whether single atoms or nanoparticles are the true active center since the preparation of single-atom catalysts is often accompanied by nanoparticles and the inevitable atomic agglomeration during the catalysis [11–13]. There is also query that is single atom always the best for catalysis? For instance, as a favorable substitute for Pt-based materials for electrocatalytic hydrogen evolution (HER), both Ru single-atoms (Ru_s) and nanoparticles (Ru_n) have been reported for HER although with different supports [14–16]. Some reports attribute the high performance to Ru_s

supported on carbon materials and carbon nitride [17–19]. Whereas, other studies showed that Ru_n also exhibits promising HER performances [20–22]. There are also reports that both Ru_s and Ru_n are beneficial to the HER [23]. It is still a big challenge to reveal the mechanism of HER supported metal catalyst and answer the question of is single atom omnipotent for catalyst development. To solve this, choosing the right support material is critical since it must provide strong metal support interactions (MSI) for stabilizing metals and retaining their high dispersion under harsh conditions, as well as modifying the catalytic properties of metals through electronic modulation [24,25].

Herein, for the first time, we developed a novel 3D porous nickel metaphosphate [$\text{Ni}_2(\text{PO}_3)_4$] (denoted as NPO) as support for HER Ru catalysts. Ru_s , Ru clusters (Ru_c) and Ru_n are controllable synthesized on NPO (Fig. 1a) to reveal the influence of Ru size on HER activities. We found that the HER activity of Ru_n is better than that of Ru_s in this Ru-

* Corresponding authors.

E-mail addresses: xjz_hmily@163.com (J. Zhao), wztzheng@jlu.edu.cn (W. Zheng), xqcui@jlu.edu.cn (X. Cui).

<https://doi.org/10.1016/j.apcatb.2022.122331>

Received 4 November 2022; Received in revised form 5 December 2022; Accepted 26 December 2022

Available online 27 December 2022

0926-3373/© 2022 Elsevier B.V. All rights reserved.

NPO system. Ru_n with bigger size has lower valence (+1.38) and optimized Ru-H bond strength, and possesses more suitable hydrogen adsorption free energy (ΔG_{H^*}) than Ru_s and Ru_c . Meanwhile, NPO also provides a unique MSI differ from other supports such as Ni_2P and graphene, which effectively regulating the local charge environment around Ru, and accelerating the water-dissociation kinetics in sluggish Volmer step [26–29]. Ru_n -NPO exhibits small overpotentials at 10 mA cm^{-2} (23.3 mV in acid, 35.4 mV in neutral, and 35.9 mV in alkaline media). Ru_n -NPO shows 21.4 times higher mass activity (MA) and 85.6 times higher price activity (PA) than 20% Pt/C catalyst under alkaline media. Additionally, NPO can firmly anchored Ru metals to ensure their even distribution and avert aggregation during the long-term reactions [30], thus endow Ru_n -NPO extraordinary stability for more than 200 h of electrolysis. This work firstly identifies that the Ru_n possess higher HER activity than Ru_s in Ru -NPO system, which provide a new direction for the catalysts design and mechanism analysis.

2. Experimental section

2.1. Preparation of Ru_s -NPO, Ru_c -NPO, Ru_n -NPO and NPO

The catalysts were synthesized by a simple two-step method. Firstly, the precursors were obtained in hydrothermal step, followed by the calcination under high temperature in tube furnace. The only difference in synthesizing Ru_s -NPO, Ru_c -NPO and Ru_n -NPO was the amount of $\text{RuCl}_3 \cdot x\text{H}_2\text{O}$. More details could be found in the [Supporting Information](#).

2.2. Electrochemical measurements

The electrochemical tests include electrochemical impedance

spectroscopy (EIS), cyclic voltammetry (CV), linear sweep voltammetry (LSV) were carried out with CHI 760E electrochemical workstation (CH Instruments, Inc., Shanghai) in a standard three-electrode system. Details are given in the [Supporting Information](#).

2.3. Material characterizations

The as-prepared catalysts were characterized by using a combination of analytical techniques, including Fourier-transform infrared (FTIR), transmission electron microscopy (TEM) and high-angle annular dark-field scanning transmission electron microscopy (HAADF-STEM), scanning transmission electron microscopy energy dispersive X-ray spectroscopy (STEM-EDS), inductively coupled plasma-optical emission spectrometry (ICP-OES), X-ray photoelectron (XPS) and the X-ray absorption fine structure spectra (XAFS). Details are presented in the [Supporting Information](#).

2.4. Computational methods

All the spin-polarized density functional theory (DFT) calculations were performed by using the Vienna Ab Initio Simulation Package (VASP), in which the electrons and ions interactions were described by the projector augmented wave (PAW) potential. The exchange-correlation interactions were treated using generalized gradient approximation (GGA) combined with Perdew, Burke, Ernzerhof (PBE) functional. More details could be found in the [Supporting Information](#).

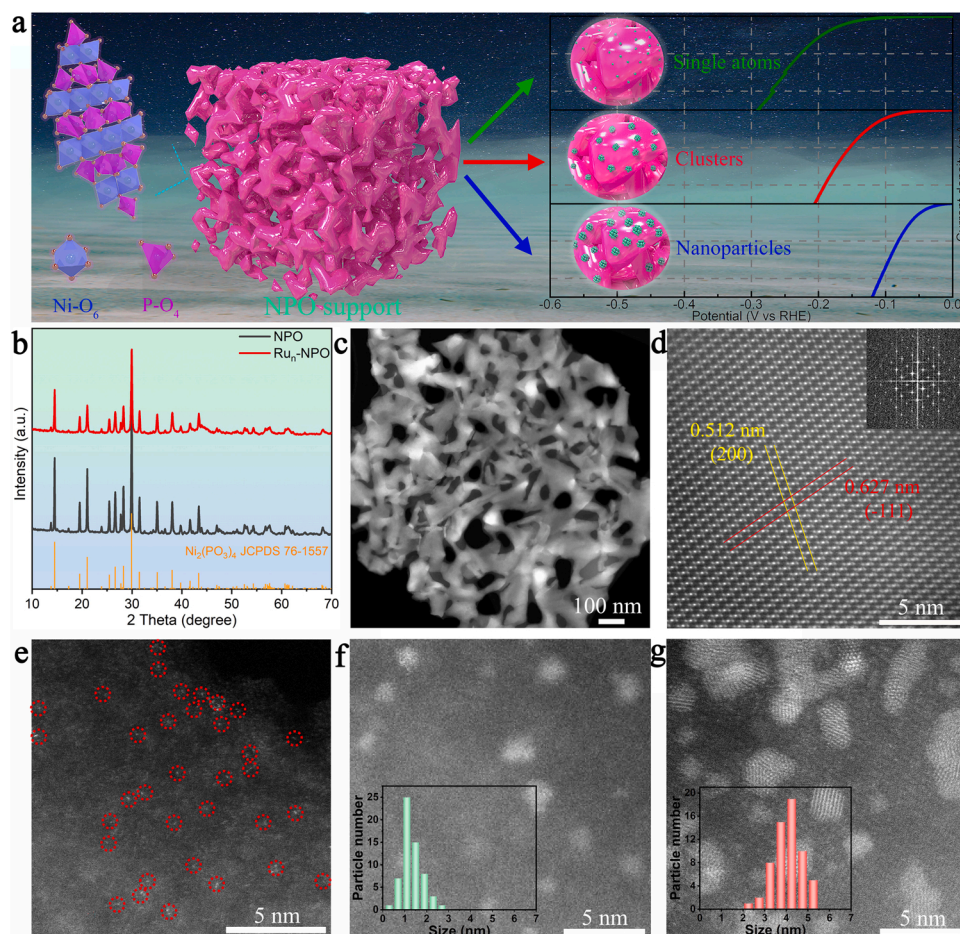


Fig. 1. (a) Schematic illustration of the structure of NPO and NPO supported Ru catalysts of single atoms, clusters, and nanoparticles with corresponding HER activities. (b) XRD patterns of the as-prepared NPO and Ru_n -NPO. (c) HAADF-STEM image of NPO. (d) HRTEM image of NPO and the corresponding FFT pattern. High-resolution HAADF-STEM images of (e) Ru_s -NPO, (f) Ru_c -NPO and (g) Ru_n -NPO. The Ru single atoms in (e) are marked by red circles. The insets in (f) and (g) give the Ru particle size distribution.

3. Results and discussion

3.1. Synthesis and characterization

The samples (NPO, Ru_s-NPO, Ru_c-NPO and Ru_n-NPO) were synthesized on carbon cloth (CC) through a simple two-step method. First, Ni and NiRu hydroxide nanosheets precursors are uniformly grown on CC by a hydrothermal method (Figs. S1, S2). Then, the final products are obtained after a phosphorization reaction. The Ru content was measured to be of 0.98 wt%, 1.34 wt% and 2.63 wt% for Ru_s-NPO, Ru_c-NPO and Ru_n-NPO, respectively (Table S1). X-ray diffraction (XRD) was used to analyze the crystal structure of the obtained products (Figs. 1b, S3). All peaks are well-indexed to the pure phase of monoclinic NPO (JCPDS no. 76–1557). Peaks for Ru crystal were not observed due to the low content. There are no peak position shifts between NPO and Ru_s-NPO, Ru_c-NPO, Ru_n-NPO. Rietveld refined XRD profile fits further indicate that there are no lattice parameter differences associated with Ru size (Fig. S4, Table S2). These results suggest that the Ru is not incorporated into the lattice, but are anchored on NPO surface. Theoretical calculations related to the formation energy were carried out (Fig. S5). The formation energy of Ru_n on the NPO surface (−5.29 eV) is much lower than those of Ru atoms doped (0.34 eV) or loaded (−2.89 eV) into NPO.

This shows that while some Ru can perhaps be loaded into NPO, this is energetically unfavorable and that Ru atoms are more likely to be distributed on NPO surface [23]. In any case, Fourier-transform infrared spectra further confirm the purity of NPO by probing the vibrational state of constituent polyanionic units (Fig. S6) [31,32].

HAADF-STEM and SEM images depict the 3D framework structure for both NPO and Ru_n-NPO (Figs. 1c, S7, S8). High-resolution TEM (HRTEM, Fig. 1d) shows that the interplanar distances of the NPO are 0.512 and 0.627 nm, in good agreement with the (200) and (−111) facet of the monoclinic NPO phase, respectively. The corresponding fast-Fourier transform (FFT) pattern is clearly visible. Ru_s, Ru_c and Ru_n can be obtained on NPO by varying the Ru loading amount. This is as shown in the HAADF-STEM images (Figs. 1e–g, S9). The bright spots marked by red circles in Fig. 1e are the atomically dispersed Ru_s. Ru_c with no obvious lattice structure and an average size of 1.33 nm are observed (Fig. 1f) as Ru content is increased. Finally, at high loading Ru_n with good crystallinity and average particle size of 4.07 nm are uniformly dispersed on NPO (Figs. 1g, S10). The interplanar distance of 0.22 nm is assigned to the (111) facet of Ru (Fig. S9f) [33]. The elemental composition and distribution on Ru_n-NPO were studied by STEM imaging and energy-dispersive X-ray spectroscopy (EDX) elemental mapping images. These show a homogenous distribution of Ni, O, P and Ru

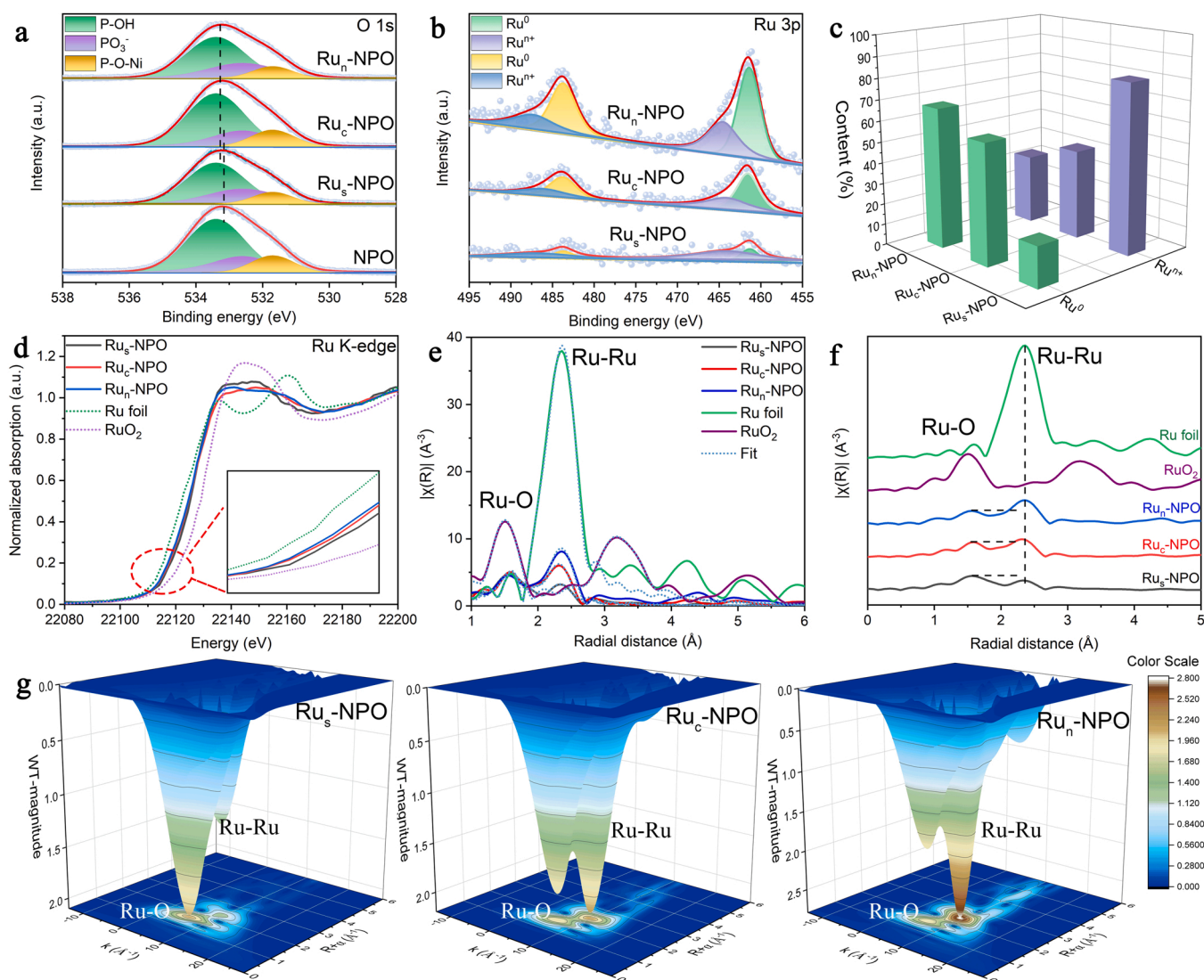


Fig. 2. (a) The O 1s XPS spectra in NPO, Ru_s-NPO, Ru_c-NPO and Ru_n-NPO. (b) The Ru 3p XPS spectra of Ru_s-NPO, Ru_c-NPO and Ru_n-NPO. (c) The corresponding Ru⁰ and Ruⁿ⁺ content in Ru_s-NPO, Ru_c-NPO and Ru_n-NPO. (d) Ru K-edge XANES spectra of Ru_s-NPO, Ru_c-NPO, Ru_n-NPO, Ru foil and RuO₂. (e, f) EXAFS k₃χ(R) spectra and the fit results of Ru_s-NPO, Ru_c-NPO, Ru_n-NPO, Ru foil and RuO₂. (g) Wavelet transforms for k₂-weighted Ru K-edge EXAFS in Ru_s-NPO, Ru_c-NPO and Ru_n-NPO.

throughout the material framework (Fig. S11). EDX line scans across the edge of Ru_n-NPO (Fig. S12) and Ru_n (Fig. S13) further confirm that the bright nanoparticles on NPO surface are Ru_n.

The electron transfer, oxidation states difference and chemical composition in NPO, Ru_s-NPO, Ru_c-NPO and Ru_n-NPO were probed by XPS. The O 1s spectra can be deconvoluted into three kinds of binding (Fig. 2a). The binding energies (BE) at ~531.7 eV, ~532.6 eV and ~533.4 eV are separately assigned to Ni-P-O, PO₃ and P-OH, respectively. The existence of PO₃ also indicates the successful synthesis of NPO [26,34]. As compared with NPO, the O 1s BE in Ru_s-NPO, Ru_c-NPO and Ru_n-NPO are positively shifted by ~0.28 eV, indicating that electrons transfer from the NPO support to Ru (Fig. S14) [35]. The Ru 3p spectra (Fig. 2b) show BE at ~462.4 eV, which belongs to Ru⁰, and a higher BE at ~464.7 eV, which can be attributed to Ruⁿ⁺ (here n + indicates additional charge) [36]. Interestingly, as shown in Fig. 2c, the proportion of Ruⁿ⁺ decreases in bigger Ru size. Ru_n-NPO possesses 33.2% Ruⁿ⁺ content, but Ru_s-NPO possesses 80.7% Ruⁿ⁺. Thus, the valence state of Ru is highly dependent on its dispersion size. The P 2p spectra can also be deconvoluted into three kinds bindings namely Ni-P-O at ~133.8 eV, PO₃ at ~134.6 eV and H₃PO₄ at ~135.2 eV (Fig. S15) [37]. In Ni 2p spectra (Fig. S16), the BE at ~856.4 eV and ~857.1 eV are attributed to Ni 2p_{3/2} and Ni 2p_{1/2}, respectively, corresponding to Ni³⁺ [38]. There are no BE shifts in the P 2p and Ni 2p spectra when comparing NPO with Ru_n-NPO, indicating that O atoms may be the bridge between Ru and NPO. This is as might be expected considering the structure of NPO, which has P coordinated by O with strong bonds exposing O. To verify the unique electronic structure between Ru and NPO, Ru_n-CC and Ru_n-Ni₂P are synthesized using the same two-step method with that of Ru_n-NPO for comparison (Fig. S17). The Ru 3p spectra of Ru_n-CC, Ru_n-Ni₂P and Ru_n-NPO are shown in Fig. S18a. Obviously, the binding energy in Ru_n-NPO are positively shifted by ~0.58 eV than those in Ru_n-CC and Ru_n-Ni₂P, indicating a higher Ru valence state in Ru_n-NPO. Specifically, the Ru⁰ content in Ru_n-CC and Ru_n-Ni₂P are 76.9% and 74.1%, respectively, which is higher than that of 66.8% in Ru_n-NPO. These results indicating that the Ru in Ru_n-CC and Ru_n-Ni₂P are more like metallic Ru, as mentioned above, metallic Ru is not conducive to the water dissociation. As for the XPS spectra of Ni₂P and Ru-Ni₂P (Fig. S19), no significant differences could be detected between the two samples, indicating the Ru_n and Ni₂P possess weak electron interaction.

X-ray absorption near-edge structure (XANES) and extended X-ray absorption fine structure (EXAFS) analyses were performed to further investigate the electronic structure and local coordination environment of the samples. Ru K-edge XANES spectra are shown in Fig. 2d. The absorption edges of Ru_s-NPO, Ru_c-NPO and Ru_n-NPO are between those of Ru foil and RuO₂, and the valence state of Ru_n-NPO is the lowest. This is in good agreement with the XPS results. Ni K-edge XANES spectra show that there is no shift of the valence state of Ni (Fig. S20a), again confirming that the structure of the NPO is not changed by Ru loading. The Fourier-transformed Ni K-edge EXAFS shows Ni-O/P as expected, and in particular no indication of a Ni-Ru bond in Ru_n-NPO (Fig. S20b). To further elucidate the interaction between Ru and NPO, the EXAFS of Ru K-edge and model-based EXAFS fitting were performed (Figs. 2e, S21, Table S3). The main peak at ~2.4 Å is associated with Ru-Ru scattering. The other peak with lower intensity at ~1.5 Å is assigned to Ru-O scattering [39], indicating that Ru are bonded with O. More specifically, in the magnified EXAFS image (Fig. 2f), the intensity of Ru-Ru scattering of Ru_s-NPO is weaker than that of Ru-O. The coordination number (C.N.) for Ru-Ru is ~1.0, indicating the presence of atomically dispersed Ru_s in Ru_s-NPO. The Ru-Ru C.N. of Ru_c-NPO and Ru_n-NPO are ~2.0 and ~4.9, respectively, which is consistent with the gradually increasing Ru cluster size. Importantly, the Ru-Ru bond distance of Ru_c-NPO (2.63 Å) and Ru_n-NPO (2.66 Å) are shorter than that of Ru foil (2.68 Å). This may in part reflect contraction of small clusters relative to bulk, but is also consistent with the observation of charge transfer due to the MSI. The wavelet transform of Ru K-edge EXAFS

confirms that there is progressively enhanced Ru-Ru scattering at ~2.4 Å from Ru_s-NPO, Ru_c-NPO to Ru_n-NPO (Fig. 2g). Notably, the Ru-Ru scattering in Ru_s-NPO is quite weak, supporting the existence of atomically dispersed Ru_s in Ru_s-NPO.

3.2. The influences of Ru size effect on HER activities

The HER catalytic activity shows a significant dependence on the Ru size. As depicted in LSV curves (Fig. 3a), the overpotential at 10 mA cm⁻² current density (η_{10}) is in the order of Ru_s-NPO (η_{10} = 112.9 mV) > Ru_c-NPO (η_{10} = 64.4 mV) > Ru_n-NPO (η_{10} = 23.3 mV). Thus the HER activities are in the following order: Ru_s-NPO < Ru_c-NPO < Ru_n-NPO, which meaning the Ru_n with bigger Ru size is most active. To eliminate the effect of Ru content on the catalytic performance, turnover frequency (TOF) value and the MA are calculated. As shown in Figs. 3b and S22, Ru_n-NPO shows the highest TOF value, and the MA (mg_{Ru}⁻¹) of Ru_n-NPO is 3.8 times higher than that of Ru_s-NPO, indicating that the activity of unit mass of Ru in Ru_n is higher than that of in Ru_s and Ru_c. Nevertheless, the HER performance will not further improved when the Ru loading amount exceeds 2.63 wt% (Fig. S23). We infer that within a certain Ru loadings, the Ru valence states modulated by strong MSI and the Ru size in Ru-NPO system play a key role in regulating HER activities. The Ru_s on NPO with its higher oxidation state is not conducive to HER. In contrast, Ru_n-NPO has a better Ru valence states of approximately + 1.38 from this point of view. To fundamentally reveal the relationship between HER activity and Ru size, three theoretical models with different amounts of Ru atoms, namely Ru₁-NPO, Ru₃-NPO and Ru₆-NPO, were developed on the basis of the experimental results (especially the C.N. in EXAFS fitting) to study the relationship between HER activity and Ru size (Fig. S24). We computed the crystal orbital Hamilton population (COHP) between the Ru site and adsorbed H* to gain more intuitive insight into the nature of bonding of the adsorbed H* (ΔE_{H^*}) among these catalysts, then, integrating the COHP up to Fermi level (ICOHP) [40]. Note that a more negative ICOHP induces stronger ΔE_{H^*} , which can also quantitatively evaluate the H* adsorption strength [41]. As shown in Fig. 3c, the orbital interaction between H* and Ru sites in Ru₆-NPO is lower than that of others, which results in a moderate adsorption energy for H* and thus enhanced catalytic activity. Then ΔG_{H^*} is used as an HER activity descriptor (the HER catalytic activity is superior when ΔG_{H^*} is close to zero) [42]. The ΔG_{H^*} values for Ru₁-NPO and Ru₃-NPO are - 0.41 eV and - 0.28 eV, respectively (Fig. 3d), the high values suggest that Ru₁-NPO and Ru₃-NPO still have a strong H* adsorption capacity and prejudice the H₂ desorption, which cause the inferior HER activities. In contrast, Ru₆-NPO has a near zero ΔG_{H^*} value (0.08 eV), indicates that Ru₆-NPO with bigger Ru size and suitable valence state is more favorable to the H* adsorption and H₂ release. Interestingly, we found that there is a linear correlation between the calculated ΔG_{H^*} and the calculated Ru charge (e⁻) as shown in the dark dots in Fig. 3e. The experimental results of valence states and the C.N. calculated from XANES also exhibit a nearly linear relationship (red stars in Fig. 3e). The correlation of two fitting lines indicates that the HER performance is modulated by the Ru valence states that highly depends on the metal size due to the strong MSI between Ru and NPO and related charge transfer.

3.3. HER activities in all pH values

We turn now to the question of whether Ru_n-NPO can exhibit satisfactory HER performance in the context of all pH. Firstly, the relevant samples are test in 0.5 M H₂SO₄ (pH=0) as shown in Fig. 4a. NPO without loading exhibits an inferior HER activity with η_{10} = 155.6 mV and 78.6 mV dec⁻¹ Tafel slope (Fig. 4b). Ru_n-NPO exhibits the best HER activity that needs η_{10} = 23.3 mV with 27.5 mV dec⁻¹ Tafel slope, which is even better than that of commercial Pt/C (η_{10} = 25.1 mV, Tafel slope: 36.6 mV dec⁻¹). The smaller EIS result for Ru_n-NPO as compared to pristine NPO also indicates fast intrinsic charge transfer at the interface

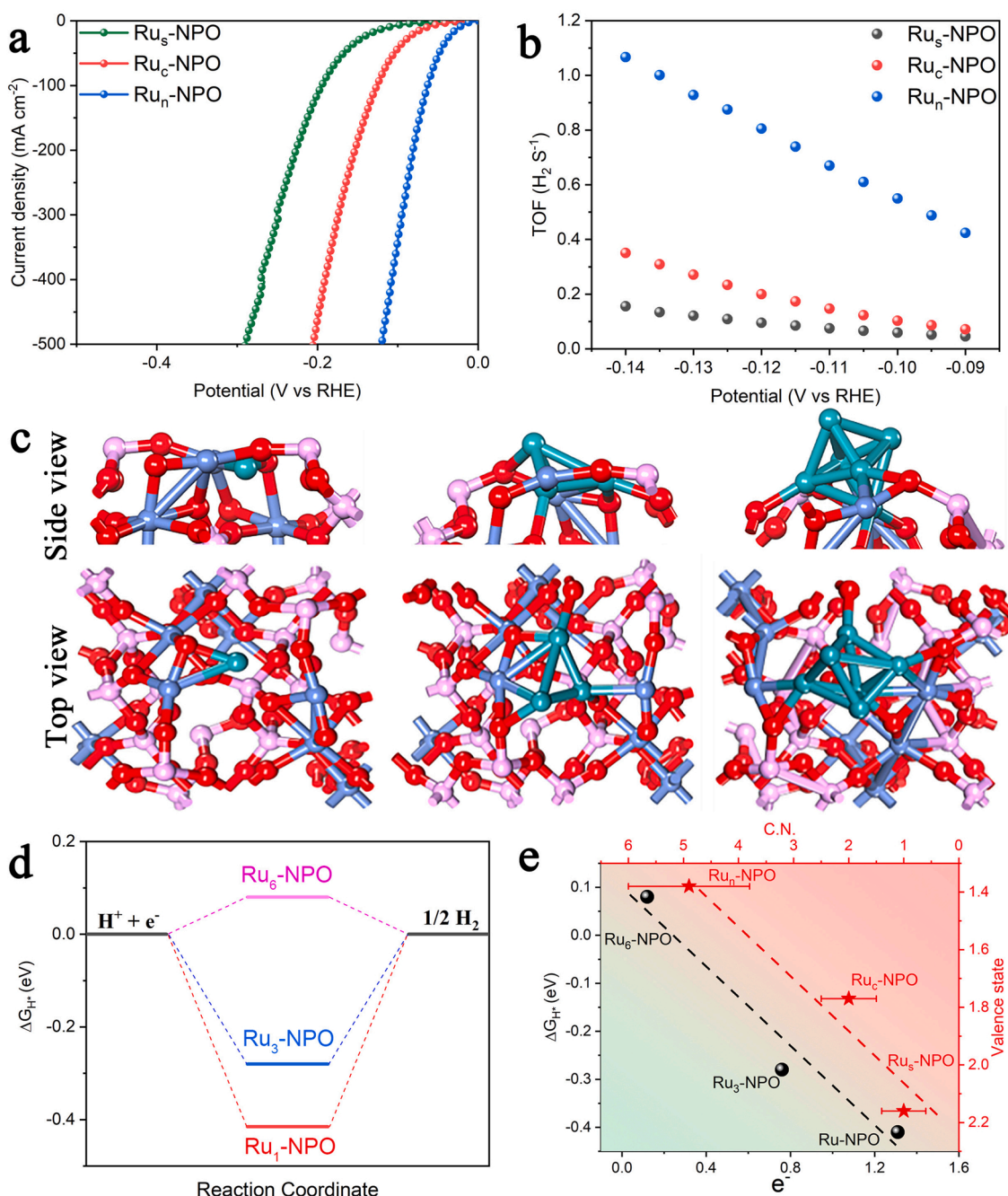


Fig. 3. (a) The polarization curves of the Ru₅-NPO, Ru₆-NPO and Ru₁-NPO in 0.5 M H₂SO₄ (pH=0). (b) TOF values of Ru₅-NPO, Ru₆-NPO and Ru₁-NPO. (c) The COHP of H⁺ on Ru site and the relationship between ICOHP and ΔE_{H^+} . The bonding and antibonding states in ICOHP are depicted by yellow and cyan, respectively. (d) Calculated values of ΔG_{H^+} for Ru₁-NPO, Ru₃-NPO and Ru₆-NPO. (e) Correlation among the calculated ΔG_{H^+} and e^- , experimental results of the Ru valence states and C. N. with error bar in different samples.

of electrocatalyst and electrolyte (Fig. S25). To verify that the high activity is derived from the unique MSI between Ru and NPO, Ru_n-CC and Ru_n-Ni₂P are used for comparison (Fig. S26). The results show that the HER activities of Ru_n-CC and Ru_n-Ni₂P are inferior to that of Ru_n-NPO. The Ru_n-NPO exhibits a smaller Tafel slope which indicating that the reaction kinetic of Ru_n-NPO is better than the others. Besides, the smallest Nyquist plots curve show a better electrical conductivity of Ru_n-NPO. It is well known that metal nanoparticles tend to dissolve in the continuous HER processes in acid media. The stability of Ru_n-CC, Ru_n-Ni₂P and Ru_n-NPO was compared by continuous LSV tests as shown in Fig. 4c. After 20 sweeps, both Ru_n-CC, Ru_n-Ni₂P show the significant activities degradation, in sharp contrast, the HER curve shows negligible

difference after 20 sweeps for Ru_n-NPO, which prove that NPO can firmly anchor Ru metals and prevents them from dissolving.

Ru_n-NPO also exhibits exceptional HER performances in neutral conditions. Neutral solutions (1 M PBS, pH=7) usually suffer from very low electrical and ionic conductivity. Encouragingly, as shown in Fig. 4d and S27, Ru_n-NPO (η_{10} = 35.4 mV, Tafel slope: 39.5 mV dec⁻¹) still exhibits better activity and reaction kinetics than Pt/C (η_{10} = 43.2 mV, Tafel slope: 44.2 mV dec⁻¹). The similar EIS semicircle with that of Pt/C indicates excellent conductivity of Ru_n-NPO in neutral solution (Fig. S28).

We further tested the HER performance of Ru_n-NPO in alkaline solutions (1 M KOH, pH=14) as shown in Fig. 4e. Remarkably, Ru_n-NPO

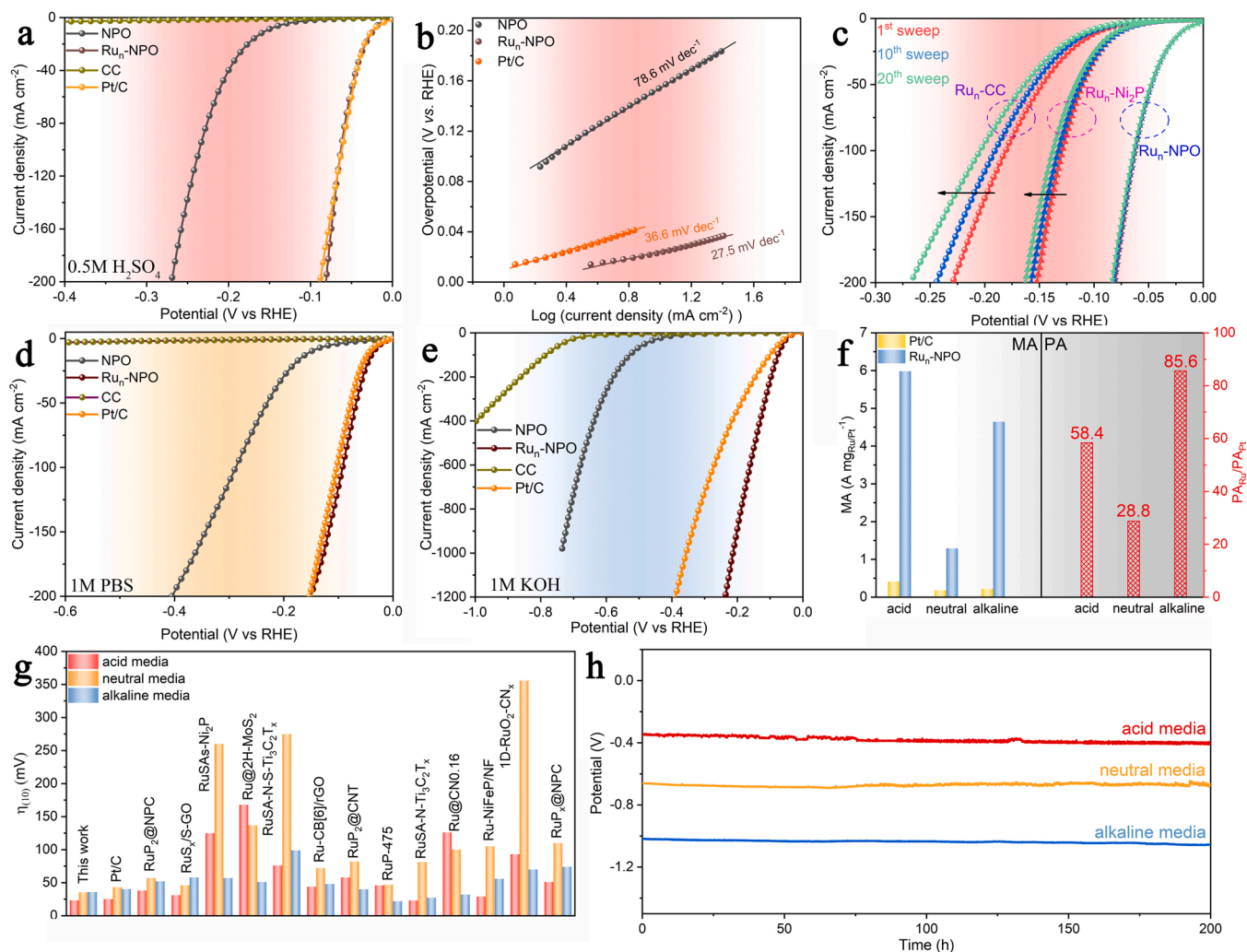


Fig. 4. (a) The HER polarization curves of the samples in 0.5 M H₂SO₄. (b) The corresponding Tafel slopes of the samples. (c) HER polarization curves of the Ru_n-CC, Ru_n-Ni₂P and Ru_n-NPO for 1st, 10th and 20th sweeps in 0.5 M H₂SO₄. (d) The HER polarization curves of the samples in 1 M PBS. (e) The polarization curves of the samples in 1 M KOH. (f) The comparing histogram of the MA of Ru and Pt at the overpotential of 200 mV (left), the red column represents the ratio of the PA of Ru to that of Pt (right). (g) The comparing histogram of overpotentials at η₁₀ in different solutions between Ru_n-NPO and other reported electrocatalysts. (h) The chronopotentiometric curves of Ru_n-NPO in all pH ranges.

shows much better HER activity ($\eta_{10} = 35.9$ mV, Tafel slope: 35.5 mV dec⁻¹) than that of Pt/C ($\eta_{10} = 40.3$ mV, Tafel slope: 43.9 mV dec⁻¹). In addition, compared with pristine NPO ($\eta_{10} = 379.5$ mV, Tafel slope: 149.8 mV dec⁻¹) (Fig. S29), the greatly reduced Tafel slope and the smaller diameter of the EIS semicircle illustrates the modified reaction kinetics and fast charge transfer of Ru_n-NPO (Fig. S30). The capacitance of the double-layer (C_{dl}) was calculated using CV. This was used to estimate the electrochemically active surface area (Fig. S31). The Ru_n-NPO catalyst also shows the greatest C_{dl} value (28 mF cm⁻²). This indicates better proton exchange between active sites and the electrolyte. The catalytic efficiency was then evaluated by TOF values (Figs. S32, S33). The TOF value for Ru_n-NPO is 1.438 s⁻¹ at 200 mV, which is nearly 2.8 times higher than that of Pt/C (0.517 s⁻¹) at the same overpotential, indicating the highest catalytic efficiency of Ru_n-NPO.

It is of interest to compare the MA between Ru in Ru_n-NPO and Pt in Pt/C. The MA of Ru in Ru_n-NPO (A mg_{Ru}⁻¹) and Pt in Pt/C (A mg_{Pt}⁻¹) are calculated (Figs. 4f, S34). The MA of Ru_n-NPO is ~ 5.985 A mg_{Ru}⁻¹, ~ 1.292 A mg_{Ru}⁻¹, and ~ 4.644 A mg_{Ru}⁻¹ in acid, neutral and alkaline media at an overpotential of 200 mV, respectively. These values are ~ 14.6 , ~ 7.2 and ~ 21.4 times higher than that of Pt/C (~ 0.409 A mg_{Pt}⁻¹, ~ 0.179 A mg_{Pt}⁻¹ and ~ 0.217 A mg_{Pt}⁻¹ in acid, neutral and alkaline media, respectively). In view of the low cost of Ru (1/4 the price of Pt), as shown

in the red columns in Fig. 4f, the price activity (PA, A dollar⁻¹) for Ru_n-NPO is ~ 58.4 , ~ 28.8 and ~ 85.6 times higher than that of Pt/C in acid, neutral and alkaline media, respectively. This combined with the stability noted above indicates potential usefulness in practical applications. Furthermore, the HER activities of Ru_n-NPO are better than those of recent reported electrocatalysts in all pH values (Fig. 4g, Table S4). Continuous CV scans and chronopotentiometry methods were used for stability test of Ru_n-NPO in all pH ranges. Ru_n-NPO exhibits negligible activity differences compared with the initial one after 2000 CV scans in acid, neutral and alkaline media (Fig. S35). Meanwhile, it shows long-term stability over 200 h at the current density of 10 mA cm⁻² in all pH ranges (Fig. 4h). The structure and morphology of Ru_n-NPO shows very slight changes after the stability test based on the results of XRD, XPS and TEM (Figs. S36–S40).

3.4. First-principles calculations on unique support effect of NPO

We performed DFT calculations to identify the thermodynamic features that lead to the exception all pH HER activity in Ru_n-NPO. The Ru₆-NPO and two other models, including Ru₆-graphene and Ru₆-Ni₂P, were chosen for comparison to indicate the unique MSI in Ru_n-NPO (Figs. S41–S45). The charge density differences were computed as

shown in Fig. 5a. Based on Bader charge analysis, $\sim 0.31\text{ e}^-$ are transferred from NPO to Ru, which is larger than that transfer from graphene (0.26 e^-) and Ni_2P (0.20 e^-) to Ru. This is consistent with the XPS analysis. Thus, NPO is identified as a better electron donor than the other two, which could be beneficial to the electron-obtaining HER process. Furthermore, the ε_d value of the freestanding Ru (111) is -1.43 eV (Fig. S46). However, after being anchored on NPO, graphene, and Ni_2P , the ε_d values of Ru are computed to be -1.87 eV , -1.55 eV and -1.37 eV , respectively, as shown in Fig. 5b. Clearly, as compared with others, the ε_d of Ru in $\text{Ru}_6\text{-NPO}$ is far away from the Fermi energy level, thus weakening the adsorption strength for H^* [43].

We then calculated the H^* adsorption and HER reaction pathways on individual Ru (111), $\text{Ru}_6\text{-graphene}$, $\text{Ru}_6\text{-NPO}$ and $\text{Ru}_6\text{-Ni}_2\text{P}$ in all pH conditions. As depicted in Fig. 5c, Ru (111) and $\text{Ru}_6\text{-Ni}_2\text{P}$ have a much stronger H^* adsorption with the ΔG_{H^*} of $\sim 0.50\text{ eV}$. In sharp contrast, $\text{Ru}_6\text{-NPO}$ exhibits a much weaker adsorption strength for H^* with a near zero ΔG_{H^*} ($\sim 0.08\text{ eV}$), suggesting the significant advantages of NPO in effectively weakening the strong H^* adsorption of Ru metal and thus accelerating the reaction rate. Besides, a linear correlation between ε_d and ΔG_{H^*} is observed (Fig. S47), verifying the accuracy of the calculated date.

As mentioned, in neutral and alkaline conditions, the HER rate is often limited by the sluggish H_2O dissociation to provide enough H^* .

Interestingly, our DFT results show that the $\text{Ru}_6\text{-NPO}$ is better able to capture H_2O molecules due to its more negative $\Delta G_{\text{H}_2\text{O}^*}$ value (-0.26 eV) as compared to Ru (111) (0.09 eV), $\text{Ru}_6\text{-graphene}$ (-0.03 eV) and $\text{Ru}_6\text{-Ni}_2\text{P}$ (-0.21 eV) (Fig. 5d). In the following H_2O dissociation step, the H_2O dissociation barrier of $\text{Ru}_6\text{-NPO}$ significantly decreased to 0.72 eV comparing to that of Ru (111) (1.98 eV), indicating the sluggish kinetics of Ru toward H_2O dissociation in Volmer step has been speeded up through the MSI between NPO and Ru.

4. Conclusions

In conclusion, we found that the Ru_n exhibits better HER activity than that of Ru_s and Ru_c in novel Ru-NPO system, which attributed to the lower valence state, optimized Ru-H bond strength and suitable ΔG_{H^*} . The unique MSI of NPO could optimize the charge transfer, and firmly anchor the Ru_n to ensure a long time stability. DFT calculations demonstrate that NPO as an electron donor, is able to both enhance the electron density of Ru_n and lead to a negative shift of the ε_d in the Ru. This reduces the strong H adsorption of Ru metal and facilitates the dissociation of Ru-H bonds and H_2 release. This catalyst also presents accelerated kinetics in alkaline and neutral media by enhancing the H_2O capture and dissociation in the Volmer step. The present results open new directions for supported metal catalyst design toward various

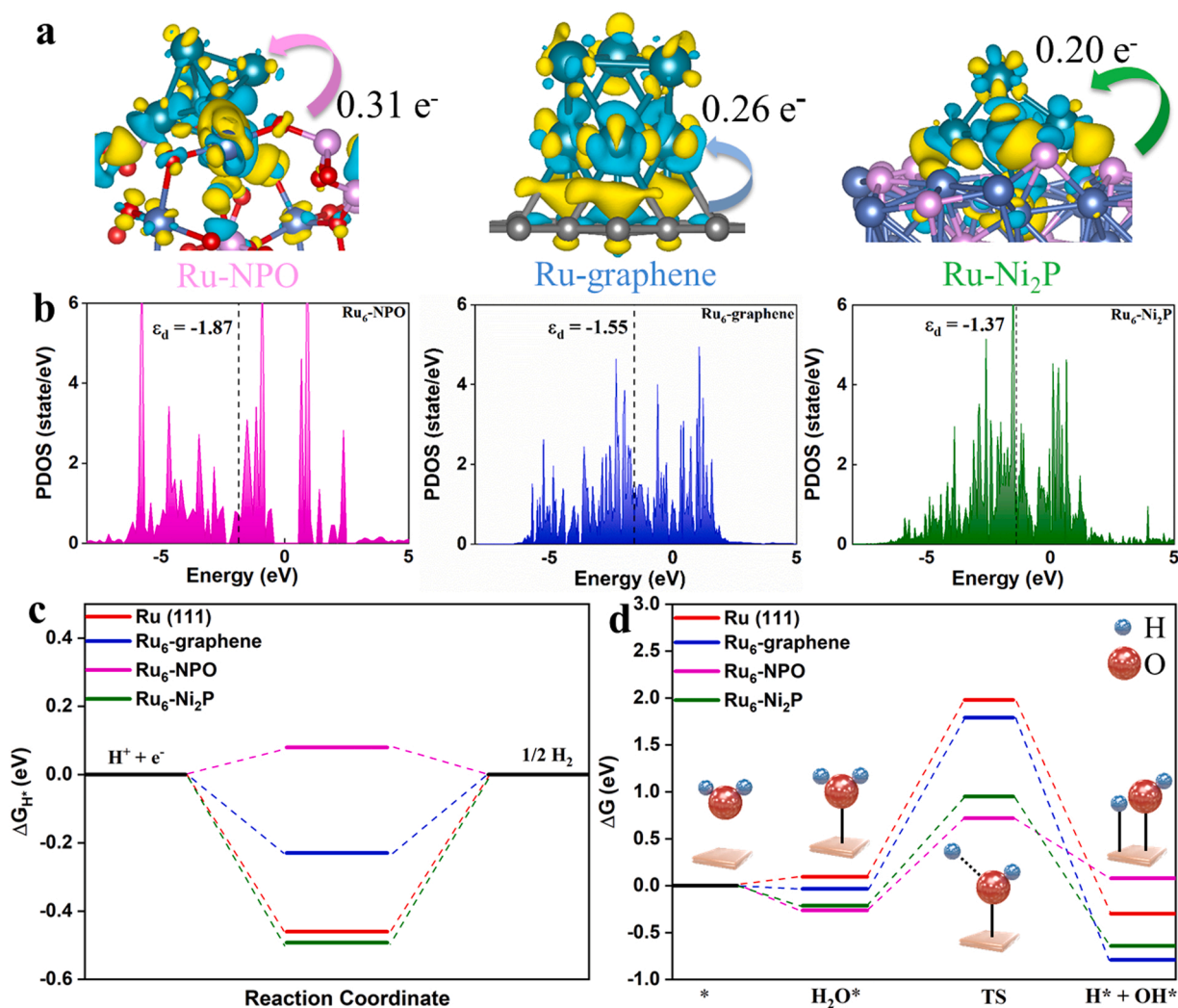


Fig. 5. (a) Electron density differences of $\text{Ru}_6\text{-NPO}$, $\text{Ru}_6\text{-graphene}$ and $\text{Ru}_6\text{-Ni}_2\text{P}$. (the yellow and sky-blue regions represent electron-rich and electron-defective, respectively). (b) Calculated electronic DOSs for $\text{Ru}_6\text{-NPO}$, $\text{Ru}_6\text{-graphene}$ and $\text{Ru}_6\text{-Ni}_2\text{P}$. (c) The chemisorption comparison of ΔG_{H^*} among the samples. (d) Reaction pathways in neutral and alkaline HER.

reactions.

CRedit authorship contribution statement

Dewen Wang: Investigation, Data curation, Resources, Writing – original draft, Writing – review & editing. **Dongxu Jiao:** Investigation, Software, Formal analysis, Resources. **Ming Gong:** Investigation, Software, Formal analysis, Resources. **Huafeng Fan:** Investigation, Software, Formal analysis, Resources. **Yuting Chen:** Investigation, Formal analysis, Resources. **Lezhi Wang:** Investigation, Formal analysis, Resources. **Jinchang Fan:** Software, Formal analysis. **Jiandong Wu:** Software, Formal analysis. **David J. Singh:** Writing – original draft, Writing – review & editing. **Jingxiang Zhao:** Software, Resources, Writing – original draft. **Weitao Zheng:** Writing – original draft. **Xiaoqiang Cui:** Software, Formal analysis, Writing – original draft, Funding acquisition.

Declaration of Competing Interest

The authors declare that they have no known competing financial interests or personal relationships that could have appeared to influence the work reported in this paper.

Data availability

Data will be made available on request.

Acknowledgments

This study was supported by the National Natural Science Foundation of China (51872116, 12034002, 22202080), the Jilin Province Science and Technology Development Program (20210301009GX), and the fellowship of China Postdoctoral Science Foundation (2022M711296). The work was carried out at LvLiang Cloud Computing Center of China, and the calculations were performed on TianHe-2.

Appendix A. Supplementary information

Supplementary data associated with this article can be found in the online version at [doi:10.1016/j.apcatb.2022.122331](https://doi.org/10.1016/j.apcatb.2022.122331).

References

- [1] A. Wang, J. Li, T. Zhang, Heterogeneous single-atom catalysis, *Nat. Rev. Chem.* 2 (2018) 65–81.
- [2] C. Dong, Z. Gao, Y. Li, M. Peng, M. Wang, Y. Xu, C. Li, M. Xu, Y. Deng, X. Qin, F. Huang, X. Wei, Y.-G. Wang, H. Liu, W. Zhou, D. Ma, Fully exposed palladium cluster catalysts enable hydrogen production from nitrogen heterocycles, *Nat. Catal.* 5 (2022) 485–493.
- [3] P. Liu, Y. Zhao, R. Qin, S. Mo, G. Chen, L. Gu, D.M. Chevrier, P. Zhang, Q. Guo, D. Zang, B. Wu, G. Fu, N. Zheng, Photochemical route for synthesizing atomically dispersed palladium catalysts, *Science* 352 (2016) 797–800.
- [4] B. Qiao, A. Wang, X. Yang, L.F. Allard, Z. Jiang, Y. Cui, J. Liu, J. Li, T. Zhang, Single-atom catalysis of CO oxidation using Pt₁/FeO_x, *Nat. Chem.* 3 (2011) 634–641.
- [5] L. Li, W. Yu, W. Gong, H. Wang, C.-L. Chiang, Y. Lin, J. Zhao, L. Zhang, J.-M. Lee, G. Zou, Sulfur-induced electron redistribution of single molybdenum atoms promotes nitrogen electroreduction to ammonia, *Appl. Catal. B Environ.* 321 (2023), 122038.
- [6] A. Mosallanezhad, C. Wei, P. Ahmadian Koudakan, Y. Fang, S. Niu, Z. Bian, B. Liu, T. Huang, H. Pan, G. Wang, Interfacial synergies between single-atomic Pt and CoS for enhancing hydrogen evolution reaction catalysis, *Appl. Catal. B Environ.* 315 (2022), 121534.
- [7] K. Qi, X. Cui, L. Gu, S. Yu, X. Fan, M. Luo, S. Xu, N. Li, L. Zheng, Q. Zhang, J. Ma, Y. Gong, F. Lv, K. Wang, H. Huang, W. Zhang, S. Guo, W. Zheng, P. Liu, Single-atom cobalt array bound to distorted 1T MoS₂ with ensemble effect for hydrogen evolution catalysis, *Nat. Commun.* 10 (2019) 5231.
- [8] Y. Wang, B. Zhu, B. Cheng, W. Macyk, P. Kuang, J. Yu, Hollow carbon sphere-supported Pt/CoO_x hybrid with excellent hydrogen evolution activity and stability in acidic environment, *Appl. Catal. B Environ.* 314 (2022), 121503.
- [9] F. Kraushofer, G.S. Parkinson, Single-atom catalysis: insights from model systems, *Chem. Rev.* (2022).
- [10] X. Mu, X. Gu, S. Dai, J. Chen, Y. Cui, Q. Chen, M. Yu, C. Chen, S. Liu, S. Mu, Breaking the symmetry of single-atom catalysts enables an extremely low energy barrier and high stability for large-current-density water splitting, *Energy Environ. Sci.* (2022).
- [11] Z. Li, S. Ji, Y. Liu, X. Cao, S. Tian, Y. Chen, Z. Niu, Y. Li, Well-defined materials for heterogeneous catalysis: from nanoparticles to isolated single-atom sites, *Chem. Rev.* 120 (2020) 623–682.
- [12] X. Han, X. Ling, Y. Wang, T. Ma, C. Zhong, W. Hu, Y.J.A.C. Deng, Generation of nanoparticle, atomic-cluster, and single-atom cobalt catalysts from zeolitic imidazole frameworks by spatial isolation and their use in zinc-air batteries, *Angew. Chem. Int. Ed.* 131 (2019) 5413–5418.
- [13] R. Bliem, J.E.S. van der Hoeven, J. Hulva, J. Pavelec, O. Gamba, P.E. de Jongh, M. Schmid, P. Blaha, U. Diebold, G.S. Parkinson, Dual role of CO in the stability of subnano Pt clusters at the Fe₃O₄ (001) surface, *Proc. Natl. Acad. Sci. USA* 113 (2016) 8921–8926.
- [14] S.-Y. Bae, J. Mahmood, I.-Y. Jeon, J.-B. Baek, Recent advances in ruthenium-based electrocatalysts for the hydrogen evolution reaction, *Nanoscale Horiz.* 5 (2020) 43–56.
- [15] C. Rong, X. Shen, Y. Wang, L. Thomsen, T. Zhao, Y. Li, X. Lu, R. Amal, C. Zhao, Electronic structure engineering of single-atom Ru sites via Co–N₄ sites for bifunctional pH-universal water splitting, *Adv. Mater.* 34 (2022) 2110103.
- [16] F. Li, G.-F. Han, H.-J. Noh, I. Ahmad, I.-Y. Jeon, J.-B. Baek, Mechanistically assisted synthesis of a Ru catalyst for hydrogen evolution with performance superior to Pt in both acidic and alkaline media, *Adv. Mater.* 30 (2018) 1803676.
- [17] J.N. Tiwari, A.M. Harzandi, M. Ha, S. Sultan, C.W. Myung, H.J. Park, D.Y. Kim, P. Thangavel, A.N. Singh, P. Sharma, S.S. Chandrasekaran, F. Salehnia, J.-W. Jang, H.S. Shin, Z. Lee, K.S. Kim, Hydrogen evolution: high-performance hydrogen evolution by Ru single atoms and nitrided-Ru nanoparticles implanted on N-doped graphitic sheet, *Adv. Energy Mater.* 9 (2019) 1970101.
- [18] J. Zhang, P. Liu, G. Wang, P.P. Zhang, X.D. Zhuang, M.W. Chen, I.M. Weidinger, X. L. Feng, Ruthenium/nitrogen-doped carbon as an electrocatalyst for efficient hydrogen evolution in alkaline solution, *J. Mater. Chem. A* 5 (2017) 25314–25318.
- [19] B. Lu, L. Guo, F. Wu, Y. Peng, J.E. Lu, T.J. Smart, N. Wang, Y.Z. Finfrock, D. Morris, P. Zhang, N. Li, P. Gao, Y. Ping, S. Chen, Ruthenium atomically dispersed in carbon outperforms platinum toward hydrogen evolution in alkaline media, *Nat. Commun.* 10 (2019) 631.
- [20] Y. Zheng, Y. Jiao, Y. Zhu, L.H. Li, Y. Han, Y. Chen, M. Jaroniec, S.-Z. Qiao, High electrocatalytic hydrogen evolution activity of an anomalous ruthenium catalyst, *J. Am. Chem. Soc.* 138 (2016) 16174–16181.
- [21] W. Li, Y. Liu, M. Wu, X. Feng, S.A.T. Redfern, Y. Shang, X. Yong, T. Feng, K. Wu, Z. Liu, B. Li, Z. Chen, J.S. Tse, S. Lu, B. Yang, Carbon-quantum-dots-loaded ruthenium nanoparticles as an efficient electrocatalyst for hydrogen production in alkaline media, *Adv. Mater.* 30 (2018) 1800676.
- [22] J. Mahmood, F. Li, S.-M. Jung, M.S. Okyay, I. Ahmad, S.-J. Kim, N. Park, H. Y. Jeong, J.-B. Baek, An efficient and pH-universal ruthenium-based catalyst for the hydrogen evolution reaction, *Nat. Nanotechnol.* 12 (2017) 441.
- [23] C. Hu, E. Song, M. Wang, W. Chen, F. Huang, Z. Feng, J. Liu, J. Wang, Partial-single-atom, partial-nanoparticle composites enhance water dissociation for hydrogen evolution, *Adv. Sci.* 8 (2021) 2001881.
- [24] Z. Chen, X. Zeng, X. Li, Z. Lv, J. Li, Y. Zhang, Strong metal phosphide–phosphate support interaction for enhanced non-noble metal catalysis, *Adv. Mater.* 34 (2022) 2106724.
- [25] L. Lin, J. Liu, X. Liu, Z. Gao, N. Rui, S. Yao, F. Zhang, M. Wang, C. Liu, L. Han, F. Yang, S. Zhang, X.-d. Wen, S.D. Senanayake, Y. Wu, X. Li, J.A. Rodriguez, D. Ma, Reversing sintering effect of Ni particles on γ -Mo₂N via strong metal support interaction, *Nat. Commun.* 12 (2021) 6978.
- [26] J. Huang, Y. Sun, Y. Zhang, G. Zou, C. Yan, S. Cong, T. Lei, X. Dai, J. Guo, R. Lu, Y. Li, J. Xiong, A new member of electrocatalysts based on nickel metaphosphate nanocrystals for efficient water oxidation, *Adv. Mater.* 30 (2018) 1705045.
- [27] R. Gond, R.P. Rao, V. Pralong, O.I. Lebedev, S. Adams, P. Barpanda, Cubic sodium cobalt metaphosphate [NaCo(PO₃)₃] as a cathode material for sodium ion batteries, *Inorg. Chem.* 57 (2018) 6324–6332.
- [28] X. Liu, B. Wen, R. Guo, J. Meng, Z. Liu, W. Yang, C. Niu, Q. Li, L. Mai, A porous nickel cyclotetraphosphate nanosheet as a new acid-stable electrocatalyst for efficient hydrogen evolution, *Nanoscale* 10 (2018) 9856–9861.
- [29] Y. Li, Z. Wang, J. Hu, S. Li, Y. Du, X. Han, P. Xu, Metal-organic frameworks derived interconnected bimetallic metaphosphate nanoarrays for efficient electrocatalytic oxygen evolution, *Adv. Funct. Mater.* 30 (2020) 1910498.
- [30] H. Zhou, F. Yu, J. Sun, R. He, S. Chen, C.-W. Chu, Z. Ren, Highly active catalyst derived from a 3D foam of Fe(PO₃)₂/Ni₂P for extremely efficient water oxidation, *Proc. Natl. Acad. Sci. USA* 114 (2017) 5607.
- [31] H. Ettis, H. Naili, T. Mhiri, Synthesis and crystal structure of a new potassium-gadolinium cyclotetraphosphate, K₂GdP₄O₁₂, *Cryst. Growth Des.* 3 (2003) 599–602.
- [32] X. Lin, Y. Dong, Q. Kuang, D. Yan, X. Liu, W. Han, Y. Zhao, Synthesis, structural, and electrochemical properties of NaCo(PO₃)₃ cathode for sodium-ion batteries, *J. Solid State Electrochem.* 20 (2016) 1241–1250.
- [33] M. Zhao, Z. Chen, Z. Lyu, Z.D. Hood, M. Xie, M. Vara, M. Chi, Y. Xia, Ru octahedral nanocrystals with a face-centered cubic structure, {111} facets, thermal stability up to 400 °C, and enhanced catalytic activity, *J. Am. Chem. Soc.* 141 (2019) 7028–7036.
- [34] Y. Li, C. Zhao, Enhancing water oxidation catalysis on a synergistic phosphorylated nife hydroxide by adjusting catalyst wettability, *ACS Catal.* 7 (2017) 2535–2541.
- [35] L.-H. Sun, Q.-Y. Li, S.-N. Zhang, D. Xu, Z.-H. Xue, H. Su, X. Lin, G.-Y. Zhai, P. Gao, S.-I. Hirano, J.-S. Chen, X.-H. Li, Heterojunction-based electron donors to stabilize and activate ultrafine Pt nanoparticles for efficient hydrogen atom dissociation and gas evolution, *Angew. Chem. Int. Ed.* 60 (2021) 25766–25770.

- [36] D. Wang, Y. Chen, L. Fan, T. Xiao, T. Meng, Z. Xing, X. Yang, Bulk and surface dual modification of nickel-cobalt spinel with ruthenium toward highly efficient overall water splitting, *Appl. Catal. B Environ.* 305 (2022), 121081.
- [37] T. Zhai, L. Wan, S. Sun, Q. Chen, J. Sun, Q. Xia, H. Xia, Phosphate ion functionalized Co_3O_4 ultrathin nanosheets with greatly improved surface reactivity for high performance pseudocapacitors, *Adv. Mater.* 29 (2017) 1604167.
- [38] M.C. Biesinger, B.P. Payne, A.P. Grosvenor, L.W.M. Lau, A.R. Gerson, R.S.C. Smart, Resolving surface chemical states in XPS analysis of first row transition metals, oxides and hydroxides: Cr, Mn, Fe, Co and Ni, *Appl. Surf. Sci.* 257 (2011) 2717–2730.
- [39] P. Li, M. Wang, X. Duan, L. Zheng, X. Cheng, Y. Zhang, Y. Kuang, Y. Li, Q. Ma, Z. Feng, W. Liu, X. Sun, Boosting oxygen evolution of single-atomic ruthenium through electronic coupling with cobalt-iron layered double hydroxides, *Nat. Commun.* 10 (2019) 1711.
- [40] X. Guo, J. Gu, S. Lin, S. Zhang, Z. Chen, S. Huang, Tackling the activity and selectivity challenges of electrocatalysts toward the nitrogen reduction reaction via atomically dispersed biatom catalysts, *J. Am. Chem. Soc.* 142 (2020) 5709–5721.
- [41] H. Niu, Z. Zhang, X. Wang, X. Wan, C. Shao, Y. Guo, Theoretical insights into the mechanism of selective nitrate-to-ammonia electroreduction on single-atom catalysts, *Nanoscale* 31 (2021) 2008533.
- [42] J. Yu, Y. Guo, S. She, S. Miao, M. Ni, W. Zhou, M. Liu, Z. Shao, Bigger is surprisingly better: agglomerates of larger RuP nanoparticles outperform benchmark Pt nanocatalysts for the hydrogen evolution reaction, *Adv. Mater.* 30 (2018) 1800047.
- [43] V. Pallassana, M. Neurock, L.B. Hansen, B. Hammer, J.K. Nørskov, Theoretical analysis of hydrogen chemisorption on Pd(111), Re(0001) and $\text{Pd}_{\text{ML}}/\text{Re}(0001)$, $\text{Re}_{\text{ML}}/\text{Pd}(111)$ pseudomorphic overlayers, *Phys. Rev. B* 60 (1999) 6146–6154.